

# 14

---

## *Stainless Steel Sandwich Sheets with Fibrous Metal Cores*

---

**A.E. Markaki and T.W. Clyne**

### **CONTENTS**

INTRODUCTION .....	150
EXPERIMENTAL PROCEDURES .....	151
Material Production .....	151
Through-Thickness Stiffness .....	151
Through-Thickness Yield Stress.....	152
Interfacial Fracture Energy .....	153
Single Fibre Tensile Testing.....	153
Electrical Conductivity .....	153
Resistance Welding.....	153
Geometrical Representation of The Core Structure.....	154
THROUGH-THICKNESS LOADING RESPONSE .....	155
Core Stiffness.....	155
Flocked Sheet and Long Fibre In-Plane Mesh.....	155
3-D Random Fibre Array .....	155
Core Strength And Yielding Behaviour.....	160
Interfacial Fracture Energy .....	162
Fibre Pull-Out In Flocked Sheets.....	164
Fibre Fracture In The In-Plane Mesh And 3D Array.....	165
THROUGH-THICKNESS ELECTRICAL RESISTANCE OF THE CORE .....	168
Flocked Sheet.....	168
Brazed In-Plane Mesh and 3-D Array .....	169
Welding Characteristics.....	170
SUMMARY .....	172
REFERENCES .....	174

## Introduction

It has long been recognised that sandwich structures, composed of stiff outer layers held apart by a low density core, offer the potential for very high specific stiffness and other attractive mechanical properties. Most such structures are created by an assembly step of some sort, before or during component manufacture. This limits the flexibility of the production process and is relatively expensive. Nevertheless, there is considerable current interest in sandwich structures of different types, many of them based on metallic faceplates and having metal-containing cores - often made of stochastic cellular metals[1-3] or some more regular structure such as a truss assembly[4-6]. However, traditional approaches to the fabrication of the latter (eg investment casting) are cumbersome and economically unattractive. A particular case of cellular metals is those made of a metallic fibre network of some sort. A novel type of a sandwich steel sheet with a fibrous stainless steel core has recently been developed[7] based on a pair of thin ( $\sim 200 \mu\text{m}$ ) stainless steel faceplates. This material has been termed a Hybrid Stainless Steel Assembly (HSSA). It can, in principle, offer a highly attractive set of property combinations, such as low areal density, high beam stiffness, efficient energy absorption during crushing and good vibrational damping capacity. Furthermore, the overall thickness of the sheet ( $\sim 1 \text{ mm}$ ), and certain features of the core structure, are such that its processing characteristics can be comparable with those of a conventional monolithic metallic sheet. Some work has recently been published on the elastic properties[8] and interfacial delamination behaviour[9] of such material.

In addition to mechanical stiffness and strength, electrical properties are relevant, since efficient fabrication using steel sheets requires that they should be weldable, preferably by electrical resistance (spot) welding. This is considered to be highly desirable for use in the automotive industry[10]. There has been extensive work on simulation of heat and current flow during spot welding[11-14], on applied force characteristics[15] and on welding of thin monolithic metallic sheets[16]. However, there is only limited information available[17] on welding of metallic sandwich sheets with fibrous metallic cores, although there has been some work[18] on welding of vibration-damped steel. This consists of two mild steel sheets, typically 0.3 to 1 mm thick, separated by a thin layer of polymeric adhesive ( $\sim 20$  to  $500 \mu\text{m}$ ).

In the present paper, a study is presented of the mechanical and electrical properties of three different variants of HSSA material and of their welding characteristics. Experimental data are correlated with predictions based on simple analytical treatments and some conclusions are drawn about the advantages and disadvantages of the variants concerned.

## Experimental Procedures

### Material Production

Three core structures have been investigated: (a) transversely-aligned fibres bonded to the faceplates by adhesive (designated "flocked sheet"), (b) in-plane pre-fabricated sintered mesh bonded to the faceplates by adhesive or brazing ("long fibre in-plane mesh") and (c) 3-dimensional brazed fibre array ("short fibre 3-D array") brazed to the faceplates. In all three cases, the faceplates were made of 200  $\mu\text{m}$  thick 316L austenitic stainless steel. Manufacturing procedures are briefly outlined below:

- (a) **Flocked sheet.** This is made by a flocking process[7], in which short ( $\sim 1$  mm) drawn 316L stainless steel fibres, about 25  $\mu\text{m}$  in diameter, are approximately transversely aligned - see Figure 14.1a. The fibres have an austenitic / martensitic microstructure, giving them high strength, but relatively low ductility. The fibres are adhesively bonded to the faceplates, using a two-component epoxy adhesive (Araldite<sup>®</sup> 420A/B). The fibre volume fraction in the core is about 10%.
- (b) **Long fibre in-plane mesh.** This is made by bonding to the faceplates a pre-manufactured solid-state sintered mesh (Bekeart S.A.), containing 19vol.% of 25  $\mu\text{m}$  diameter fibres of 316L stainless steel, about 16 mm in length. Most of the fibres in the mesh are inclined at a relatively high angles ( $\sim 80^\circ$ ) to the vertical. The starting fibres are the same as those used in (a), but the heat treatment involved during sintering leads to complete conversion of the martensite to austenite, lowering the strength and raising the ductility. Bonding of the core to the faceplates was carried out either by adhesive bonding, using a two-component epoxy adhesive (Araldite<sup>®</sup> 420A/B), or by brazing, using a Ni-14Cr-4Fe-2.8B-3.3Si-0.6C braze alloy (Brazing & Soldering Automation Ltd) and a brazing temperature of 1100°C for a period of about 5 minutes.
- (c) **Short fibre 3-D array.** This consists of a 3-D network of fibres bonded to each other, and also to the faceplates, using the same braze alloy as for the long fibre in-plane mesh. In this case, the fibres are inclined at various angles to the vertical, with an average value of the order of 60°. They occupy about 10% of the volume of the core and are made of 446 (ferritic) stainless steel, melt extracted to lengths of 2.5 mm (product of FibreTech Ltd). These fibres have high strength, combined with limited ductility.

### Through-thickness Stiffness

The through-thickness Young's moduli of the sheets were measured using the high load head of a Micromaterials NanoTest 600 indenter. A flat -

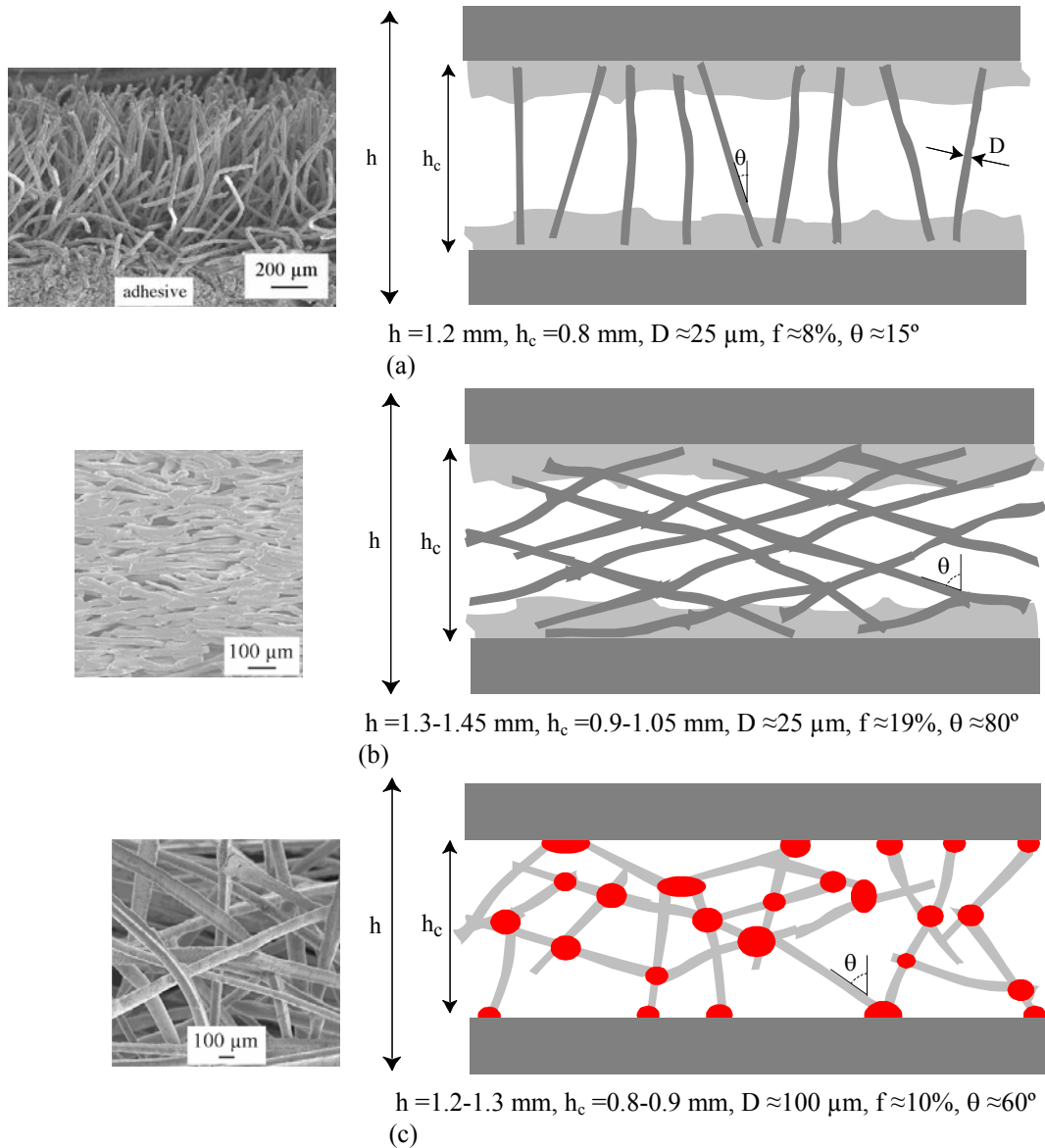


**FIGURE 14.1:** SEM micrographs showing cross-sectional view of the core and schematic depictions of the structure of (a) flocked sheet, (b) long fibre in-plane sheet, and (c) short fibre 3-D array.

ended cylindrical indenter head was used, with a diameter of 25 mm. The specimens were cut to square sections with sides of length about 5 mm. Loads of up to about 20 N were applied, corresponding to average stresses on the faceplate of around 0.8 MPa.

### Through-thickness Yield Stress

Small coupons, measuring 10 mm by 15 mm, were loaded in compression on a servo-hydraulic testing apparatus equipped with a 10 kN load cell. The tests were conducted under controlled displacement rate of

0.15 mm min<sup>-1</sup> and the through-thickness displacements were recorded from an LVDT ( $\pm 500 \mu\text{m}$  range) with a resolution of about 5  $\mu\text{m}$ . Attention was focussed on identification of the core yield stress, corresponding to the onset of substantial plastic bending and buckling among the fibres in the core.

### **Interfacial Fracture Energy**

The resistance to delamination of the face plates was measured under mode I loading conditions. The test procedure employed[19] involves bonding of the sheet to two steel plates and loading these under pure bending, so as to generate mode I crack growth. Prior to testing, a narrow pre-crack was introduced into the specimen at the mid-plane.

### **Single Fibre Tensile Testing**

Single fibre testing was carried out using a Schenk desktop testing machine, fitted with a 5 or 250 N load cell. The individual fibres were mounted on paper tabs, with a central cut-out that gave a gauge length of about 25 mm. The tab was gripped in the jaws of the testing machine and, prior to testing, cuts were made from each side to the central cut-out. The cross-head displacement was measured using an LVDT. All tests were conducted in displacement control at a rate of 0.1 mm min<sup>-1</sup>. Fibres were tested in the as-received condition and also after a heat treatment similar to those involved during solid-state sintering or brazing.

### **Electrical Conductivity**

Specimens were in the form of small rectangular coupons (10 × 14 mm). An AC circuit was used for the measurements. A fixed current (1 A) was passed through the specimen via flat ended probes on the faceplates. This current was modulated at a constant frequency of 1 kHz. The potential drop across the specimen, from which the resistivity of the core was deduced, was then amplified and measured. In making this measurement, the potential drop across other resistances in the sensing circuit must be eliminated. This drop generates an offset in the mean voltage of the AC signal. This DC offset was removed by passing the signal through an AC amplifier, after which it was rectified by a demodulator and then passed through an integrator to remove noise and finally displayed as a DC voltage (few mV to ~1 V for these specimens). Full details of the technique are given elsewhere[20].

### **Resistance Welding**

Resistance welding trials were conducted on a single phase AC machine. Cu/Cr/Zr electrodes to ISO 5821 type E design were used, having 16 mm diameter and 6 mm radius dome tip. An electrode force of 1.5 kN was

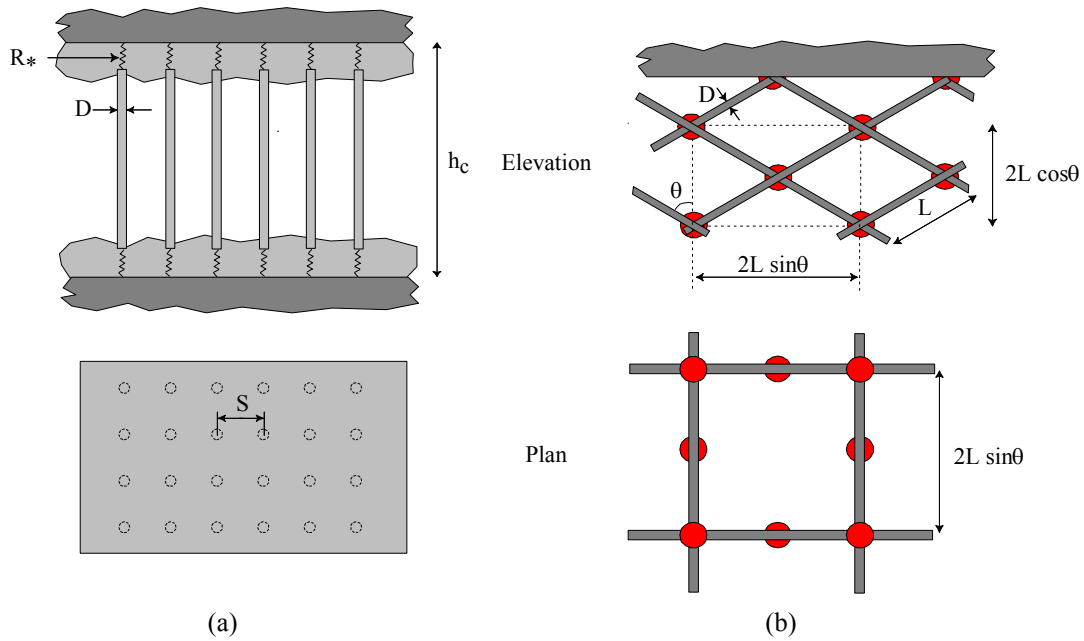


**FIGURE 14.2:** Schematic showing modeled fibre distributions for (a) the transverse fibre and (b) sintered mat (right) structures.

used. Single welds were made on small coupons. In cases where the core did not allow significant currents to flow at the low voltages used in resistance welding (typically about 5 V), a clamp tool was used to provide a current shunt path, in parallel with the electrodes, linking the outer sheet surfaces. This current flow heated the specimen sufficiently to allow deformation of the core, and hence direct flow through it, so that welding could be achieved. The welding current and voltage were measured using a standard meter and oscilloscope.

### Geometrical Representation of the Core Structure

Simple analytical models have been developed, giving the fibre volume fraction  $f$  as a function of geometrical variables. For the flocked sheet core, a square array was assumed, with side of length  $S$  (Figure 14.2a). The fibre volume fraction is thus given by

$$f = \frac{\pi D^2}{4 S^2} \tag{14.1}$$

where  $D$  is the fibre diameter. The number of fibres per unit area,  $N$ , is related to the fibre volume fraction  $f$  and the fibre diameter,  $D$

$$N = \frac{4f}{\pi D^2} \tag{14.2}$$

For the long fibre in-plane mesh, a tetragonal unit cell is identified, of side  $2L \sin\theta$  and height  $2L \cos\theta$ , where  $L$  is the length of a segment of fibre having one end at a cell corner and the other at the mid-point of a vertical face (Figure 14b). Each cell thus contains 16 fibre segments, all of which are shared between 2 cells. The fibre volume fraction and the number of fibres per unit area are thus given by

$$f = \frac{8 \left[ L \left( \frac{\pi D^2}{4} \right) \right]}{(2L \sin\theta)^2 (2L \cos\theta)} = \frac{\pi D^2}{4L^2 \sin^2\theta \cos\theta} \quad (14.3)$$

$$N = \frac{4}{(2L \sin\theta)^2} = \frac{4f \cos\theta}{\pi D^2} \quad (14.4)$$

For the short fibre 3-D array, the relationship between  $N$  and  $f$  is simply obtained by noting that, for a set of prisms with a 3-D random orientation distribution of the prism axes, the area intersected by any plane is twice the area intersected by a plane lying normal to the alignment direction of a set of parallel prisms occupying the same volume fraction[21]. Hence,  $N$  here has a value of half that for the case of an aligned set of cylinders ( $=f/(\pi D^2/4)$ ), i.e.,

$$N = \frac{2f}{\pi D^2} \quad (14.5)$$

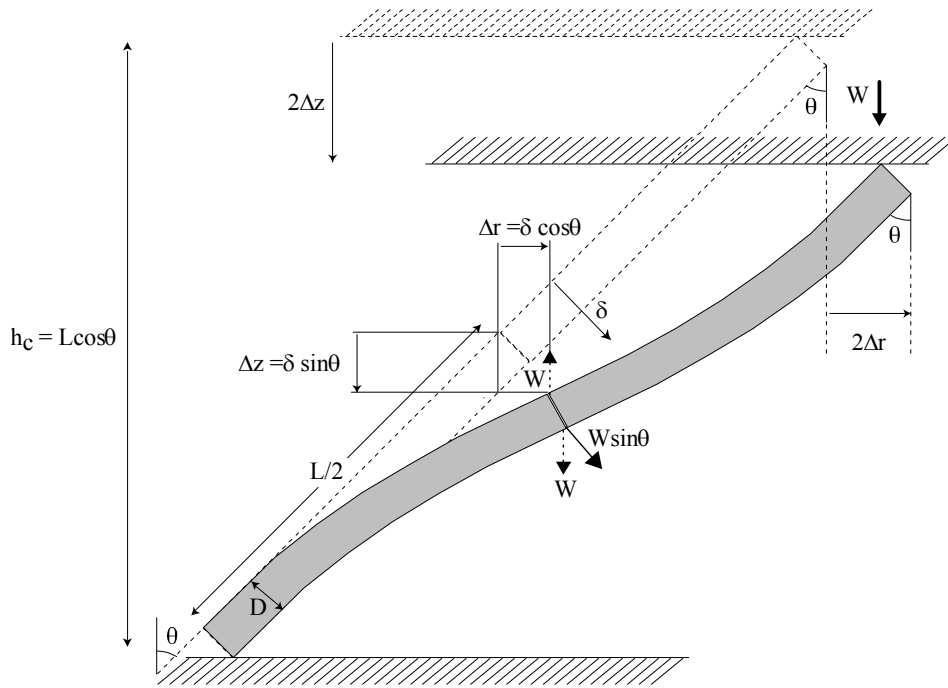
## Through-thickness Loading Response

### Core Stiffness

Two different approaches, based on a cantilever bending model, have been used to predict the through-thickness stiffness of the sandwich sheet cores. The first is applicable for the flocked sheet and long fibre in-plane mesh, in which the fibres are inclined at a specified angle, whereas the second approach assumes a three-dimensionally random orientation distribution of the fibre axes (short fibre 3-D array).

### Flocked Sheet and Long Fibre In-Plane Mesh

The Young's modulus of the core in the through-thickness direction can be predicted by considering the behaviour of a single fibre of length  $L$ , initially straight and inclined at an angle  $\theta$  to the direction of the applied load. The situation under load is depicted schematically in Figure 14.3. All fibres inclined at such an angle will behave similarly under the action


**FIGURE 14.3**

Elevation view of the elastic bending of an inclined fibre under the influence of a vertical load,  $W$ .

of an imposed load  $W$  normal to the plane of the sheet, provided any interaction between individual fibres is neglected and assuming that their behaviour remains linearly elastic. From elementary beam bending theory, the normal deflection,  $\delta$  ( $=\Delta z/\sin\theta$ ), of the free end of a cantilever beam of length  $L/2$ , subjected to a load  $W\sin\theta$  normal to the beam axis, is given by

$$\frac{\Delta z}{\sin\theta} = \frac{1}{3} \frac{W\sin\theta (L/2)^3}{E_f I} \quad (14.6)$$

where  $E_f$  is the fibre modulus and  $I$  is the moment of inertia of the fibre section ( $=\pi D^4/64$ , where  $D$  is the fibre diameter, for cylindrical fibres).

The through-thickness strain of the core,  $\varepsilon_c$ , is given by

$$\varepsilon_c = \frac{2\Delta z}{h_c} \quad (14.7)$$

Substituting for  $\Delta z$  from Equation 14.6, and writing the core thickness as  $L\cos\theta$  (see Figure 14.3), leads to

$$\varepsilon_c = \frac{2W \sin^2\theta (L/2)^3}{3E_f (\pi D^4/64) L\cos\theta} = \frac{16W \sin^2\theta L^2}{3E_f \pi D^4 \cos\theta} \quad (14.8)$$

Now, the applied pressure,  $P$ , can be expressed in terms of the value of  $W$  and the number of fibres per unit area,  $N$

$$P = NW \quad (14.9)$$

Substituting for  $N$  from Equation 14.4, the Young's modulus of the core in the through-thickness direction can be expressed as

$$E_c = \frac{P}{\varepsilon_c} = \frac{3NW E_f \pi D^4 \cos\theta}{16 W \sin^2\theta L^2} = \frac{3(4f\cos\theta) E_f \pi D^4 \cos\theta}{16(\pi D^2) \sin^2\theta L^2} = \frac{3E_f f}{4 s^2 \tan^2\theta} \quad (14.10) \quad ($$

where  $s (=L/D)$  is the fibre aspect ratio.

Predictions<sup>†</sup> obtained using Equation 14.10 show that higher stiffness is predicted for fibres inclined at low angles, as expected, since a fibre provides less resistance to vertical displacement when it is inclined at a high angle. It may also be noted that, for a given volume fraction of fibre, there will be more fibres per unit area when  $\theta$  is close to  $0^\circ$  (see Equation 14.4). Also, the fibres will be of lower aspect ratio, for a given core thickness. The net effect is cumulative, so the sensitivity of the stiffness to  $\theta$  is quite strong ( $\tan^2\theta$ ). Furthermore, it can be seen that the stiffness goes up sharply as the fibre aspect ratio is decreased. An obvious way of increasing the stiffness, for a given core thickness, is to use fibres with larger diameter. An increase in fibre content will also generate increased stiffness, but this is less efficient and, of course, it also raises the density of the core.

### 3-D Random Fibre Array

The cantilever bending model (Figure 14.3) can be also used to predict the elastic stiffness of an isotropic random fibre array. In this case, the fibre being considered does not span the two faceplates, but is just a segment between two fibre-fibre joints. The deflection is induced by an applied stress,  $\sigma$  (compressive in Figure 14.3), which generates a force  $W$  on each individual fibre segment. These are related by

$$\sigma = NW \quad (14.11)$$

where  $N$  is the number of fibre segments per unit sectional area.

---

<sup>†</sup> This treatment clearly breaks down in the limit of  $\theta=0^\circ$ , when the predicted stiffness tends to infinity. The value must be upper bounded at  $fE_f$ , corresponding to the fibres remaining vertical and being axially compressed. In practice, even this value would not be approached, at least for fibres with relatively high aspect ratios. Realistically, the model may be taken as applicable for angles down to around  $5-10^\circ$ , which is probably all that is required.

As before, the normal deflection,  $\delta$ , of the end of a cantilever beam of length  $L/2$ , subjected to a load  $W \sin\theta$  normal to the beam axis, is given by

$$\delta = \frac{W \sin\theta (L/2)^3}{3E_f \left(\frac{\pi D^4}{64}\right)} = \frac{8W \sin\theta L^3}{3E_f \pi D^4} \quad (14.12)$$

so that, substituting for  $W$  from Equations 14.11 and 14.12 and  $N$  from Equation 14.5, the axial deflection is given by

$$\Delta z = \delta \sin\theta = \frac{4\sigma L^3 \sin^2\theta}{3E_f f D^2} \quad (14.13)$$

The overall deformation expected with a material composed of a three-dimensionally random array of fibres can be analysed, at least approximately, by summing the contributions<sup>§</sup> from individual fibre segment deformations. The segments are assumed to exhibit a spherically symmetric orientation distribution, which has a  $\sin\theta$  angular probability distribution about any given axis. The expected overall relative net extension in the direction of an applied stress can therefore be written down by considering the displacements of a set of fibre mid-points, using the expression for the deflection normal to the fibre axis, as a function of the distance along the fibre, given by Equation 14.13. The macroscopic deflection in the loading direction, and hence the strain, can thus be expressed as

$$\begin{aligned} \varepsilon_c = \frac{\Delta Z}{Z} &= \frac{\int_0^{\pi/2} \Delta z \sin\theta d\theta}{\int_0^{\pi/2} z \sin\theta d\theta} = \frac{\int_0^{\pi/2} \frac{4\sigma L^3 \sin^3\theta}{3E_f f D^2} d\theta}{\int_0^{\pi/2} \left(\frac{L}{2} \cos\theta\right) \sin\theta d\theta} \\ \therefore \varepsilon_c &= \left(\frac{8\sigma}{3E_f f}\right) \left(\frac{L}{D}\right)^2 \frac{\int_0^{\pi/2} \sin^3\theta d\theta}{\int_0^{\pi/2} \cos\theta \sin\theta d\theta} = \left(\frac{32\sigma}{9E_f f}\right) \left(\frac{L}{D}\right)^2 \quad (14.14) \end{aligned}$$

---

<sup>§</sup> In reality, the deflections exhibited by individual fibre segments will be influenced by the configuration of neighbouring segments, so this analysis is clearly not rigorous when the inclination angles vary within the material. For example, the axial deflection of a segment inclined at a substantial angle to the stress axis would be reduced if a closely neighbouring segment were aligned parallel to the axis. However, such interactions are unlikely to generate large errors in the proposed model, at least for an effectively isotropic, homogeneous material.

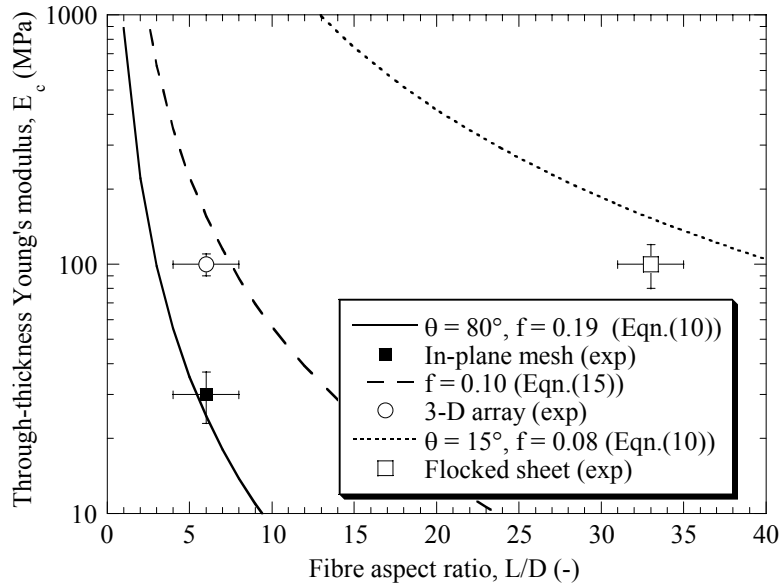


**FIGURE 14.4**

Through-thickness Young's modulus of the core as a function of fibre aspect ratio. The three points correspond to experimental measurements, while the curves are predictions obtained using Equations 14.10 and 14.15. A value of 200 GPa was used for the stiffness of the stainless steel fibres.

The Young's modulus of the fibre array,  $E_c (= \sigma/\epsilon)$ , is therefore given by

$$\therefore E_c = \frac{9E_f f}{32 \left(\frac{L}{D}\right)^2} = \frac{9E_f f}{32 s^2} \quad (14.15)$$

A comparison between experimental results and predictions obtained using Equation 14.10 (flocked sheet, long fibre in-plane mesh) and Equation 14.15 (short fibre 3-D array) is shown in Figure 14.4. It can be seen that experimental data are broadly consistent with predictions from the model predictions. For the flocked sheet, the measured value of about 100 MPa is in fairly good agreement with predictions obtained using estimated values for  $s$ ,  $f$  and  $\theta$  of 33 ( $= h_c / D \sin\theta$ ), 8% and  $15^\circ$  respectively. For the in-plane mesh, stiffnesses of the order of 30 MPa were obtained experimentally. Using estimated values for  $s$ ,  $f$  and  $\theta$  of 6, 19% and  $80^\circ$  respectively gives a predicted stiffness of about 25 MPa. For cores in which the fibres are bonded together, the appropriate aspect ratio to use is that between fibre joints: this value can be estimated from study of SEM micrographs such as that shown in Figure 14.1b. For the short fibre 3-D array, the measured value of about 100 MPa is in fairly good agreement with predictions obtained using estimated values for  $s$  and  $f$  of 6 and 10% respectively. In any event, it is clear that all of these stiffnesses are relatively low (appreciably lower, for example, than would

be the case if the cavity were filled with resin, ie  $\sim 1\text{--}3$  GPa), and that these results are broadly consistent with the model predictions.

### Core Strength and Yielding Behaviour

It's a simple matter to extend the stiffness model to predict the onset of yielding in the core. The maximum stress generated in the outer surface of the fibres is given by

$$\sigma_{f,\max} = \frac{MD}{2I} = \frac{32M}{\pi D^3} \quad (14.16)$$

where  $M$  is the bending moment ( $=W \sin\theta L/2$ ). Using Equation 14.8 to substitute for  $W$  leads to

$$\sigma_{f,\max} = \frac{32 (3E_f \pi D^4 \cos\theta \varepsilon_c) \sin\theta L/2}{\pi D^3 (16 \sin^2\theta L^2)} = \frac{3E_f \varepsilon_c}{s \tan\theta} \quad (14.17)$$

Equation 14.17 can be used to obtain an expression for the yield stress of the fibre,  $\sigma_{f,Y}$ , in terms of the through-thickness yield strain of the core  $\varepsilon_{c,Y}$

$$\sigma_{f,Y} = \frac{3E_f \varepsilon_{c,Y}}{s \tan\theta} \quad (14.18)$$

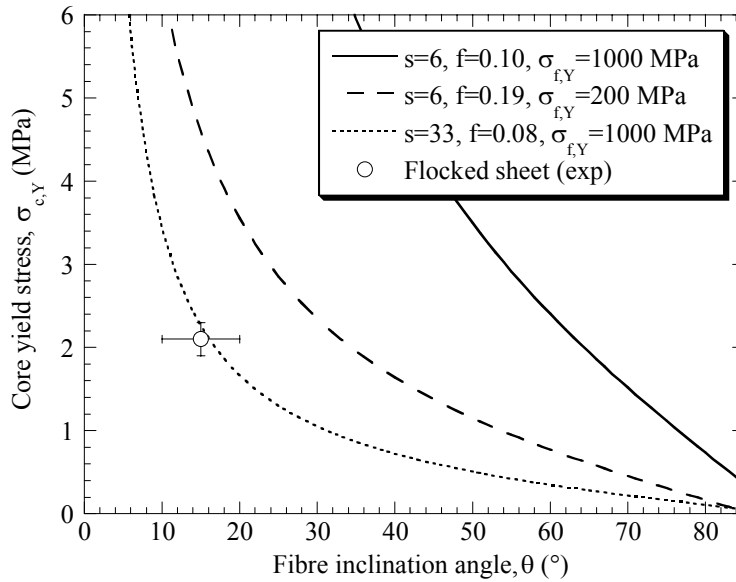
The through-thickness yielding stress of the core  $\sigma_{c,Y}$ , in turn, can be expressed as

$$\sigma_{c,Y} = E_c \varepsilon_{c,Y} \quad (14.19)$$

Substituting for  $E_c$  and  $\varepsilon_{c,Y}$ , from Equations 14.10 and 14.18, respectively,  $\sigma_{c,Y}$  can be expressed in terms of  $\sigma_{f,Y}$

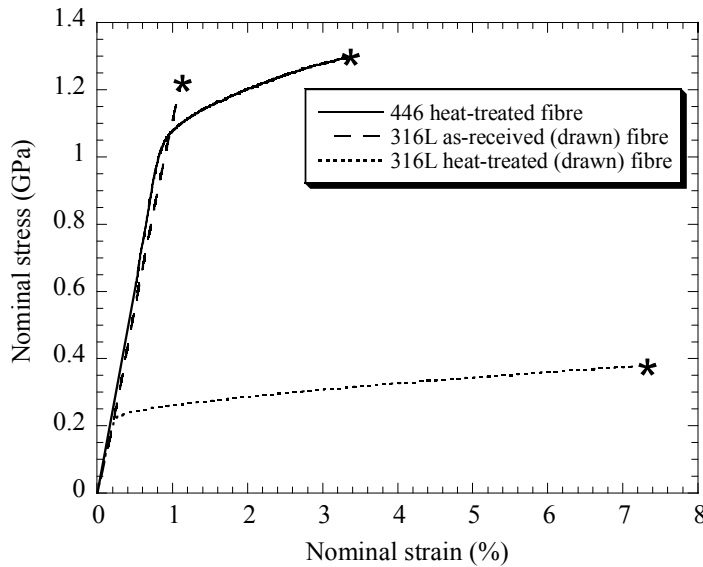
$$\sigma_{c,Y} = \frac{3E_f f}{4 s^2 \tan^2\theta} \frac{\sigma_{f,Y} s \tan\theta}{3E_f} = \frac{f \sigma_{f,Y}}{4 s \tan\theta} \quad (14.20)$$

From Equation 14.20, it can be seen that the core yielding stress rises as the fibre aspect ratio is decreased, although the dependence is not as strong as that exhibited by the stiffness. A plot is shown in Figure 14.5 of predictions from this equation for the short fibre 3-D array ( $s = 6$ ,  $f = 0.10$ ,  $\sigma_{f,Y} = 1000$  MPa), the long fibre in-plane mesh ( $s = 6$ ,  $f = 0.19$ ,  $\sigma_{f,Y} = 200$  MPa) and the flocked sheet ( $s = 33$ ,  $f = 0.08$ ,  $\sigma_{f,Y} = 1000$  MPa). The yield strengths of the heat-treated 446 (short fibre 3-D array), heat-treated 316L (in-plane mesh) and the as-received (drawn) 316L (flocked

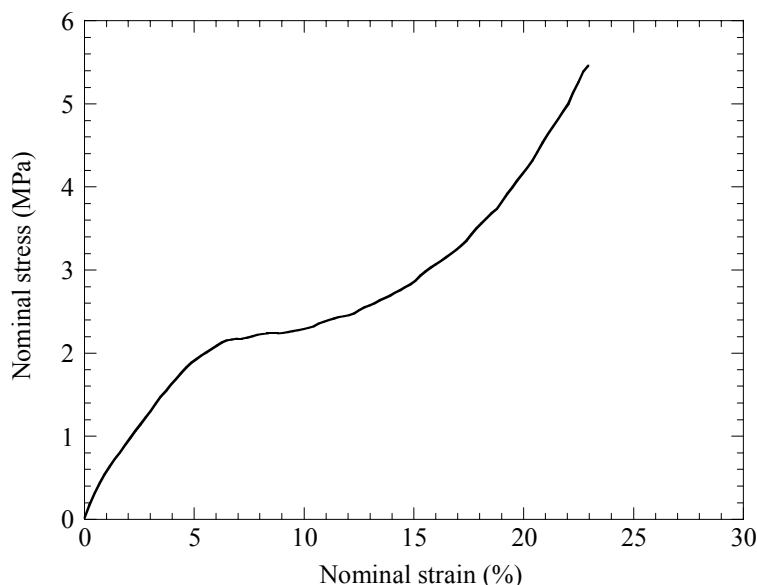


**FIGURE 14.5** Predicted dependence (Equation 14.20) of the through-thickness yield stress of the core on the fibre inclination angle. The yield strength of the fibres was obtained from the stress-strain curves of Figure 14.6. Also, plotted is the experimental result for the yield stress of the flocked core obtained from compression testing (Figure 14.7).

sheet) fibres were obtained from single fibre tensile testing (see Figure 14.6). Also plotted in Figure 14.5 is the experimentally-measured value of  $\sigma_{c,Y}$  obtained from compression of the flocked sheet, which can be inferred from Figure 14.7 to be about 2.1 MPa. It can be seen that this value is in good agreement with the model predictions.



**FIGURE 14.6** Typical single fibre tensile testing data for (a) as-received (drawn) 316L (flocked sheet), (b) heat-treated 316L (long fibre in-plane mesh) and (c) heat-treated 446 (short fibre 3-D array) fibres.

**FIGURE 14.7**

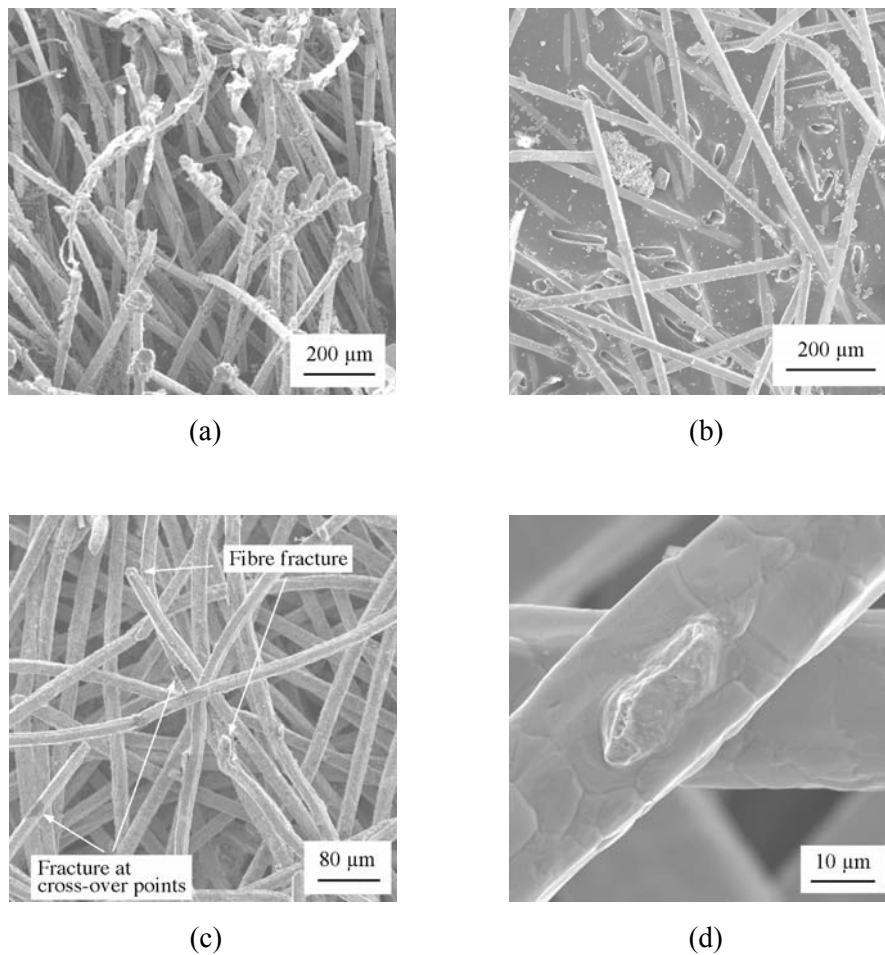
Typical stress-strain plot for compressive testing of the flocked sheet.

For the other two materials, on the other hand, it is difficult to quantify this value experimentally, at least during compression testing, because extensive yielding only occurs after substantial densification has taken place, so the compressive stress-strain curve does not display a distinct plateau regime. In practical terms, it was evident on general handling and testing of the sheets that the short fibre 3-D random core material is substantially stronger than the other two,

### Interfacial Fracture Energy

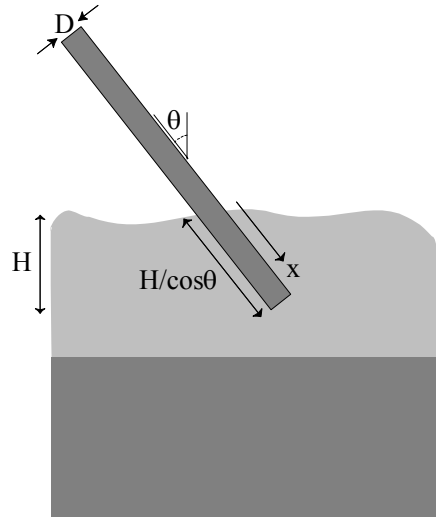
The flocked sheets were observed to delaminate predominantly by fibres being pulled out of their sockets in the adhesive layer. This is illustrated in Figure 14.8a. The measured value of the (mode I) fracture energy was found to be about  $340 \text{ J m}^{-2}$ . In contrast, the long fibre in-plane mesh and the short fibre 3-D array delaminated within the core itself, rather than at the interfaces with the faceplates. This is illustrated in Figure 14.8b for the in-plane mesh. The average measured values of the (mode I) fracture energies were about 30 and  $675 \text{ J m}^{-2}$ , respectively, for the in-plane mesh and the short fibre 3-D array. There were no systematic differences between the behaviour of the adhesively bonded and brazed in-plane mesh sheet: this is unsurprising, since they differ only in the way that the fibres are attached to the faceplates and in all cases the fracture and deformation was confined to the mid-plane region.

However, there is a substantial difference in the fracture energies between the in-plane mesh and the short fibre 3-D array. This may be attributed to the different bonding techniques employed to generate joints

**FIGURE 14.8**

SEM micrographs of fracture surfaces. The top pair are from a flocked sheet specimen, showing (a) glue adhering to the ends of pulled-out fibres and (b) sockets in the adhesive layer, from which fibres had been pulled out. The bottom pair are from a long fibre in-plane mesh, showing (c) a general view and (d) a fractured neck formed at a fibre-fibre joint.

between adjacent fibres. Solid-state sintering is a very slow process and, even after prolonged holding at high temperature, the joints are likely to be limited in area and consequently weak. Furthermore, the prolonged heating can lead to grain coarsening and extensive carbide precipitation, reducing the fibre strength. On the other hand, liquid phase sintering techniques, such as brazing, are much faster than solid state sintering, since the rate-determining process is viscous flow, rather than diffusion. Well-consolidated joints can therefore be formed quickly and readily, with less danger of deleterious changes in the fibre microstructure. Of course, the mechanical properties of the braze metal may be relevant, but with suitable joint geometry the stresses in the braze metal will be much lower than those in the fibres, making it unlikely that the joints will fail.

**FIGURE 14.9**

Schematic of the model used for prediction of energy absorption during pull-out of inclined fibres for the flocked sheet core.

### Fibre Pull-out in Flocked Sheets

A simple model has been developed for delamination in the flocked sheet, based on a shear-lag treatment of fibre pull-out[22]. Consider an inclined fibre with a diameter  $D$  and an embedded length  $x$ , as illustrated in Figure 14.9. The work done in pulling out a single inclined fibre can be written as

$$\Delta G = \int_0^{H/\cos\theta} \pi D x \tau_{i*} dx = \pi D \frac{H^2}{2\cos^2\theta} \tau_{i*} \quad (14.21)$$

where  $\tau_{i*}$  is the fibre / adhesive interfacial shear strength, taken as constant along the fibre length. If the number of fibres per unit area is written as  $N$ , there will be  $(N \cos\theta dx/H)$  per unit area with an embedded length between  $x$  and  $(x + dx)$ . Thus the total work done in pulling out the inclined fibres,  $G_{fp}$  is given by

$$G_{fp} = \int_0^{H/\cos\theta} \frac{N \cos\theta dx}{H} \pi D \frac{H^2}{2\cos^2\theta} \tau_{i*} \quad (14.22)$$

Substituting the expression for  $N$  given in Equation 14.4 into Equation 14.22 and integrating (assuming equal embedded lengths for all fibres) leads to

$$G_{fp} = \frac{2f \tau_{i*} H^2}{D \cos\theta} \quad (14.23)$$

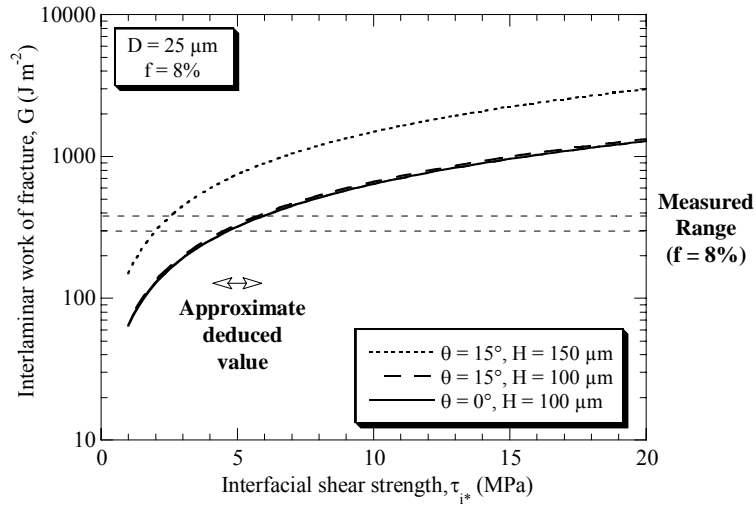


**FIGURE 14.10**

Predicted dependence (Equation 14.23) of the interlaminar fracture energy of the flocked sheet on the fibre-adhesive interfacial shear strength.

Figure 14.10 shows the predicted dependence of this pull-out energy on interfacial shear strength. From SEM images of cross-sections through the sheet, it was estimated that the fibres are typically anchored into the adhesive to a depth of about 100 μm (= *H*). It can be seen that the experimentally obtained value of *G* (~ 340 J m<sup>-2</sup>) corresponds to that predicted by the model (using *f* = 8%, *H* = 100 μm, *θ* = 15° and *D* = 25 μm) if the fibre / adhesive interfacial shear strength has a value of about 5 MPa. This is a relatively low value for an interfacial shear strength [23, 24], although it is certainly of the order of magnitude expected.

**Fibre Fracture in the In-plane Mesh and 3D Array**

The long fibre in-plane mesh and the short fibre 3D array were observed to delaminate by fibre fracture. A simple model has been developed to estimate the fracture energy for this mechanism. It is assumed that all the fibres deform and fracture within a deformation zone of length *z*. This is illustrated in Figure 14.11. The work of fracture may in this case be written as

$$G_{fr} = N U_s z \tag{14.24}$$

where *U<sub>s</sub>* is the work of fracture for a single fibre. Substituting the expression for *N* given in Equation 14.4 into Equation 14.24 leads to an expression for the work of fracture of the long fibre in-plane mesh

$$G_{fr} = \left[ \frac{4f \cos\theta}{\pi D^2} \right] U_s z \tag{14.25}$$

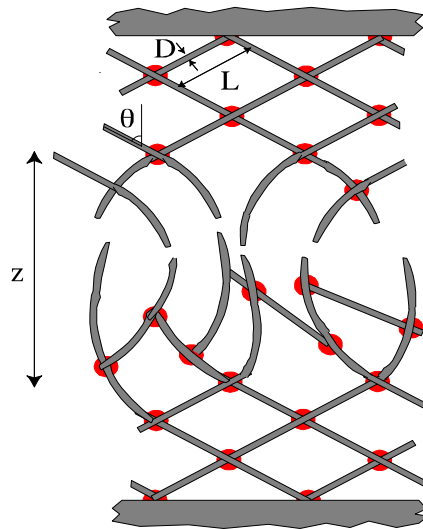


**FIGURE 14.11** Schematic of the model used for prediction of energy absorption during fibre fracture for the in-plane mesh and the 3-D array.

Predictions obtained using this equation are shown in Figure 14.12. The work of fracture for a heat-treated 316L fibre was measured from the area under the load-strain curve (Figure 14.6) and is approximately  $0.0011 \text{ J m}^{-1}$ . The experimental value of  $G$  ( $\sim 30 \text{ J m}^{-2}$ ) is consistent with model predictions if the fibres are inclined at  $85^\circ$  to the stress axis and the deformation zone is about  $100 \mu\text{m}$  long. Evidently, the length of the deformation zone is an important parameter and these results suggest that deformation is restricted to a fairly narrow band. This is not something

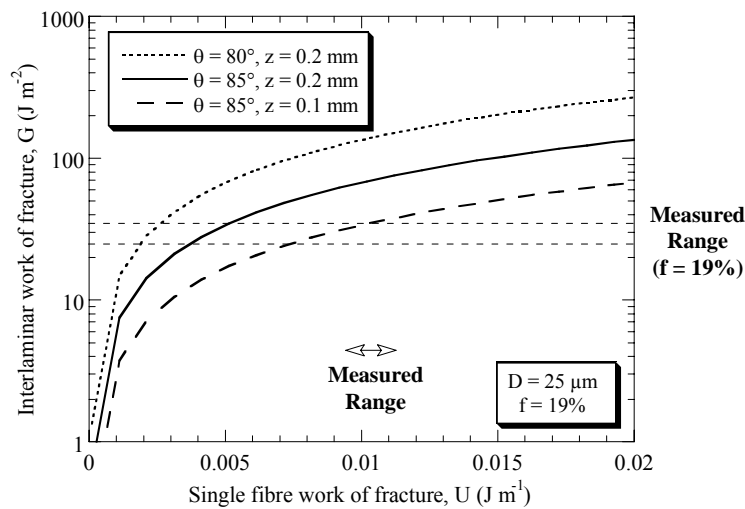


**FIGURE 14.12** Predicted dependence (Equation 14.25) of the interlaminar fracture energy of the long in-plane mesh on the single fibre work of fracture.

that can readily be verified by inspection of failed specimens, since it is rather difficult to establish precisely where substantial plastic deformation of the fibres has occurred. Nevertheless, the general impression on inspecting the damage and deformation zone is that it was wider than 100  $\mu\text{m}$ . Moreover, the value of 85° used for the fibre inclination angle is probably too high.

It can thus be seen that the experimental value is actually considerably lower than that predicted using the model. The probable explanation for this is evident in Figure 14.8c and 14.8d, where it can be seen that failure commonly occurred at the sintered necks, rather than by fibre fracture. As illustrated in Figure 14.8d, the width of the necks can be quite small, relative to the fibre diameter. Consequently, when the faceplates are torn apart, necks that are not sufficiently strong are apparently quite prone to fail. This probably accounts for the measured fracture energy values being lower than predicted.

For the short fibre 3-D array, substituting the expression for  $N$  given in Equation 14.5 into Equation 14.24 leads to the following expression for the work of fracture

$$G_{\text{fr}} = \left[ \frac{2f}{\pi D^2} \right] U_s z \quad (14.26)$$

Predictions obtained using this equation are shown in Figure 14.13. The work of fracture for a heat-treated 446 fibre was measured from the area under the load-displacement curve (Figure 14.6) and is approximately 0.2  $\text{J m}^{-1}$ . The experimental value  $G$  ( $\sim 675 \text{ J m}^{-2}$ ) broadly agrees with model predictions if the deformation zone is taken to have a length of the

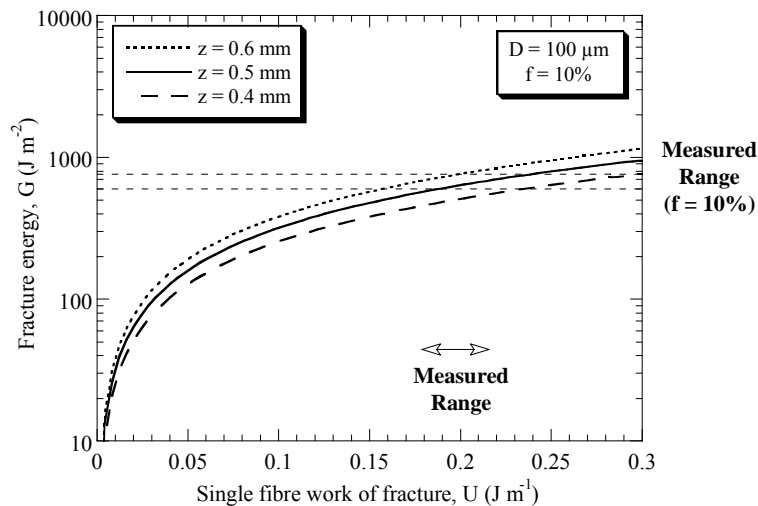


**FIGURE 14.13**

Predicted dependence (Equation 14.26) of the interlaminar fracture energy of the 3-D fibre array on the single fibre work of fracture.

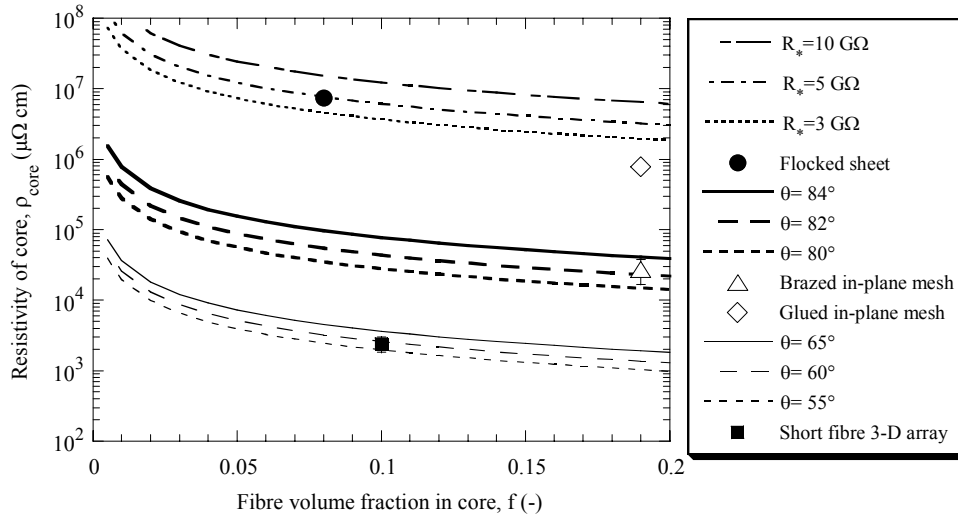


**FIGURE 14.14**

Core resistivity as a function of fibre content. Points are experimental data and curves are predictions, obtained using Equation 14.29, with three values of  $R^*$  and  $h_c = 0.8$  mm, for the flocked sheet, and Equation 14.32, with three values of  $\theta$ , for the long in-plane mesh and the short fibre 3-D array. Resistivity values of 85 and 65  $\mu\Omega$  cm, respectively, were used for the austenitic (flocked sheet and long in-plane mesh) and ferritic (short fibre 3-D array) fibres.

order of 0.5 mm (Figure 14.13). It may be noted that this is the approximate spacing between the fibre-fibre joints in this material (see Figure 14.1c).

## Through-thickness Electrical Resistance of the Core

### Flocked Sheet

For the flocked sheet, the through-thickness core resistivity was predicted assuming the fibre arrangement shown in Figure 14.2a. The resistance of a fibre column,  $R_{col}$ , is equal to the sum of the resistance offered by the fibre itself and the contact resistance at each interface with the faceplates,  $R^*$

$$R_{col} = R_{fib} + 2R^* = \frac{4 \rho_{fib} h_c}{\pi D^2} + 2R^* \quad (14.27)$$

where  $h_c$  is the separation of the faceplates ( $\sim$  fibre length) and  $\rho_{fib}$  is the fibre material resistivity. Since there is, in effect, one fibre column per square array, the apparent resistivity of the core,  $\rho_{core}$ , is given by

$$\rho_{core} = \frac{\left( \frac{4 \rho_{fib} h_c}{\pi D^2} + 2R^* \right) S^2}{h_c} \quad (14.28)$$

After substitution for  $S$  in terms of  $f$  (Equation 14.1), this leads to an expression for the core resistivity in terms of known dimensions, the resistivity of the fibre material and the contact resistance.

$$\rho_{\text{core}} = \frac{1}{f} \left( \frac{R_* \pi D^2}{2 h_c} + \rho_{\text{fib}} \right) \quad (14.29)$$

It can be seen that the thickness of the core comes into this expression.

### Brazed In-plane Mesh and 3-D Array

For the brazed in-plane mesh and the short fibre 3-D array, it is assumed that there is no contact resistance at the interface between fibres and faceplates, so the treatment just concerns a small representative volume of core material (Figure 14.2b). The resistance to current flow presented by the unit cell,  $R_{\text{cell}}$ , can be expressed in terms of the resistance of a segment of fibre  $R_{\text{seg}}$ . Since, in effect, current passes through two sets of 4 parallel segments as it progresses down the height of a unit cell, it follows that

$$\frac{1}{R_{\text{cell}}} = \frac{4}{2R_{\text{seg}}} = \frac{2}{\frac{L \rho_{\text{fib}}}{\left(\frac{\pi D^2}{4}\right)}} = \frac{\pi D^2}{2 L \rho_{\text{fib}}} \quad (14.30)$$

The resistance offered by the unit cell can also be expressed in terms of the resistivity of the core

$$R_{\text{cell}} = \frac{\rho_{\text{core}} 2L \cos\theta}{(2L \sin\theta)^2} = \frac{\rho_{\text{core}} \cos\theta}{2L \sin^2\theta} \quad (14.31)$$

Combining Equations 14.3, 14.30, and 14.31 leads to

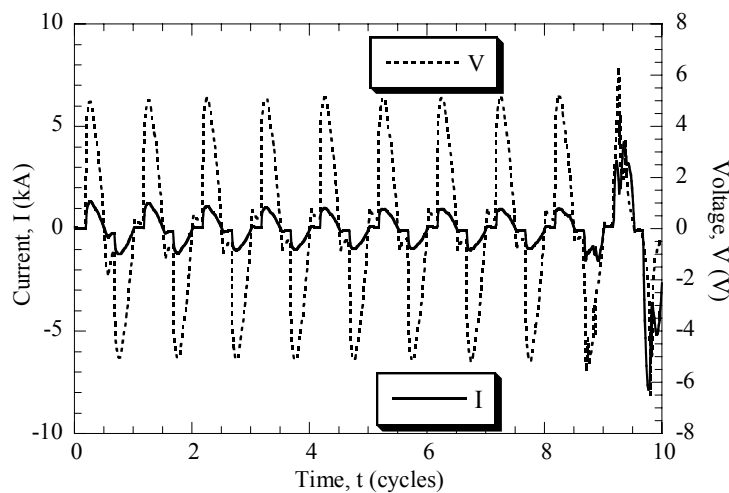
$$\rho_{\text{core}} = \frac{\rho_{\text{fib}}}{f \cos^2\theta} \quad (14.32)$$

A comparison between experimental results and predictions (Equations 14.29 and 14.32) is shown in Figure 14.14. It can be seen that, in order to obtain consistency with experimental data, it is necessary to assume a relatively high resistance (few  $G\Omega$ ) between fibre end and faceplate in the flocked fibre core. This can be attributed to poor electrical contact with the faceplates. The experimental resistivities of the brazed in-plane mesh and the short fibre 3-D array cores are orders of magnitude lower than the effective resistivity of the flocked core. The values are consistent with the simple geometrical model, assuming that

the fibres are inclined at about  $82^\circ$  and  $60^\circ$  respectively to the direction of current flow. These figures are at least approximately correct. The resistance of the adhesively bonded in-plane mesh is considerably higher than the predicted levels for a brazed sintered mat, which is attributed to poor electrical contact with the faceplates. However, it can be seen that this is still better than in the flocked material. This is probably because pressure was applied while the adhesive was setting, bringing the fibres into better electrical contact with the faceplates than is possible with the flocked sheet procedure.

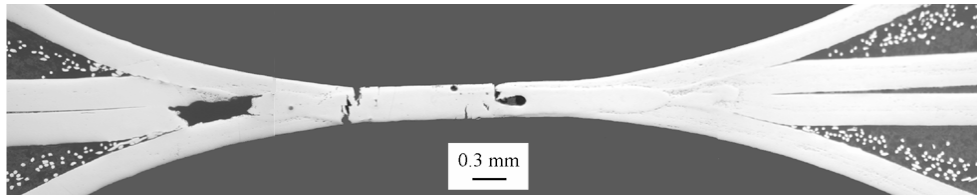
### Welding Characteristics

The flocked sheet could not be welded directly, since no significant current flowed through the material with the electrode force and voltage used. This is consistent with the high measured electrical resistivity of the core. By using a shunt, however, it was found to be possible to create a weld. Initially, sufficient current flowed through the faceplates and across the shunt to cause heating of the core between the electrodes, leading to softening, consolidation and hence sufficient reduction in core resistance to allow a substantial direct current to flow and melting to occur. However, during these initial trials, breakthrough of the core was inconsistent and the faceplates were susceptible to local burn-through by the shunt current. In the example shown in Figure 14.15, breakthrough and current increase occurred only in the last of the 10 cycles of weld time. Even then, the poor shape of the final half cycles of current indicates intermittent current flow. In some cases, depending on the position of the shunt, no breakthrough occurred at all.



**FIGURE 14.15**

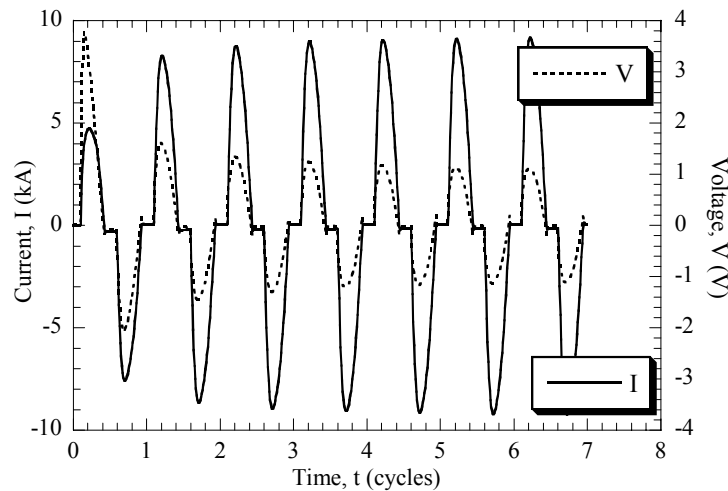
Voltage-time and current-time plots obtained during welding together of two flocked sheets, with a weld time of 10 cycles (0.2 s).

**FIGURE 14.16**

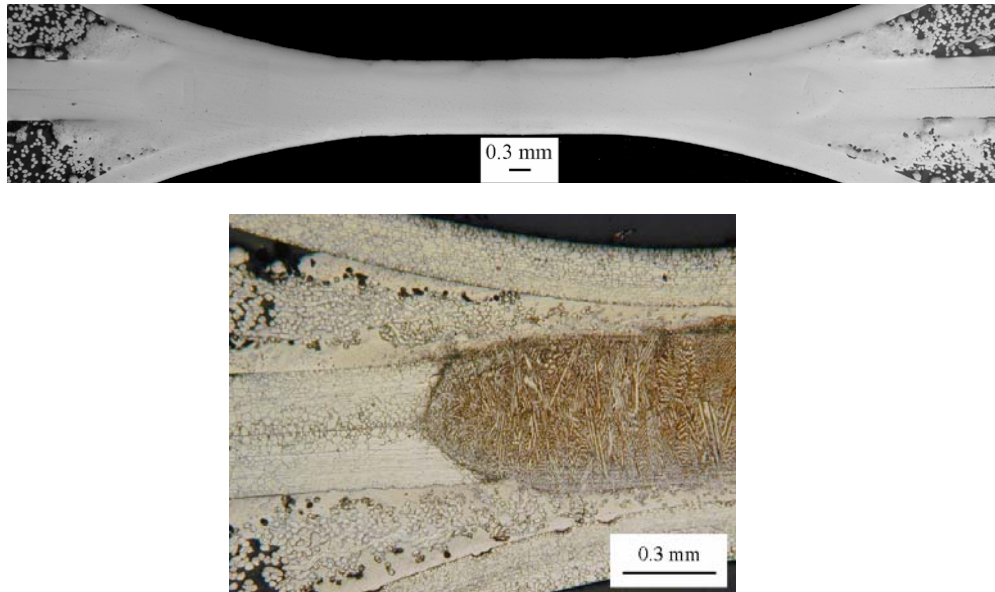
Optical micrograph of a polished transverse section from a pair of flocked sheets after resistance welding.

Even when a weld was created between flocked sheets, it was invariably of poor quality. This can be seen in the micrograph shown in Figure 14.16, where it is clear that the pressure has resulted in much of the faceplate material being melted and squeezed out laterally. There has also been vaporisation of the adhesive, leading to blow-holes, and cracking of the faceplates. Melt expulsion of this type is often problematic, particularly with thin metal sheets in composite materials such as vibration damping steels[18]. Such a weld would be mechanically very weak.

The brazed long fibre in-plane sheet, on the other hand, was readily weldable. Figure 14.17 shows typical voltage and current plots. The current rises quickly to the set value and substantial heat is generated from the start in the sheets between the electrodes. Sections through a corresponding weld are shown in Figure 14.18. It can be seen that the weld is of good quality, with some lateral flow of melted fibres, but the inner faceplates retaining their integrity and the outer faceplates remaining unmelted. The brazed short fibre 3-D array core material is also readily weldable, as expected.

**FIGURE 14.17**

Voltage-time and current-time plots obtained during welding of a pair of brazed in-plane mesh sheets, with a weld time of 7 cycles (0.14 s).

**FIGURE 14.18**

Optical micrographs of transverse sections from a pair of brazed in-plane mesh sheets after resistance welding, showing an as-polished complete section (above) and a higher magnification view of an etched sample (below), in which the fused zone is clearly visible.

---

## Summary

This chapter relates to a new sandwich sheet material (~ 1 mm thick), composed of thin stainless steel face-plates and a low density metallic fibre core. Such material can offer low areal density, high stiffness, efficient energy absorption during crushing and good acoustic / vibrational damping capacity, in combination with processing characteristics (such as formability and weldability) comparable with those of conventional metal sheet. The chapter, gives an outline of some of the relationships between core structure and relevant thermo-mechanical and electrical properties exhibited by the sheet. The following conclusions can be drawn.

- (a) Three variants of a novel, thin sandwich steel sheet, with a steel fibre core, have been characterised in terms of core structure. One variant (flocked sheet) contains strong (austenitic / martensitic) fibres oriented approximately normal to the plane of the sheet and bonded to the faceplates by adhesive. The second variant (long fibre in-plane mesh) contains solid-state sintered mats of softer (recrystallised, fully austenitic) fibres oriented at low angles to the plane of the sheet, brazed or adhesively bonded to the faceplates.

The third variant (short fibre 3-D array) contains an approximately 3-D random network of strong, melt-spun (ferritic) fibres, brazed to each other and to the faceplates. Fibre contents in the core are around 10% for the flocked sheet and the 3-D array, while the figure is about twice this for the in-plane mesh.

- (b) The measured through-thickness Young's moduli are relatively low ( $\sim 10$ - $100$  MPa) and are broadly consistent with predictions from an analytical model based on the bending of individual fibres. Core yield stress values have also been explored, and are in the range 1-10 MPa. In this context, it is worth noting that, in sandwich sheets, the bending stiffness and strength are dominated by the faceplates, so the core does not necessarily need to be very stiff or strong. However, very compliant, or very soft, cores might be problematic, in that they may allow excessive shear between the faceplates or failure to maintain faceplate separation under load, leading to low beam stiffness or premature plastic deformation of the sheet. The brazed 3-D random fibre array core performs appreciably better than the other two in this regard.
- (c) The fracture energy during delamination of the faceplates has been measured for mode I loading conditions. The flocked fibre core fails by pull-out of fibres from their sockets in the adhesive. A model has been developed to predict the energy absorbed during fibre pull-out, based on simple shear lag theory. Good agreement is found between theory and experiment, assuming an interfacial shear strength between fibre and adhesive of about 5 MPa. The long in-plane mesh and the short fibre 3-array both fail by fracture within the core. A model has been developed for prediction of the fracture energy for this type of failure, based on deformation and fracture of individual fibres. Good agreement with experiment is obtained for the short fibre 3-D array sheet, which has the highest fracture energy. Experimental values for the long fibre in-plane mesh, however, are lower than predicted. This is ascribed to a tendency for delamination to occur by failure of solid state sintered fibre-fibre necks, which are relatively weak, rather than by fibre fracture.
- (d) Through-thickness electrical resistivities have been measured for the cores of the flocked sheet ( $\sim 10 \Omega \text{ cm}$ ), adhesively bonded in-plane mesh ( $\sim 1 \Omega \text{ cm}$ ), brazed long in-plane mesh ( $\sim 0.01 \Omega \text{ cm}$ ) and the brazed short fibre 3-D array ( $\sim 0.001 \Omega \text{ cm}$ ). These values compare well with predictions from simple geometrical models. The high resistivity of the flocked fibre core is attributed to poor electrical contact between the fibre ends and the faceplates.
- (e) The flocked (adhesively-bonded) material could not readily be welded. A shunt was required to achieve any melting, but electrical contact through the core was variable. In addition, weld flaws and

faceplate damage occurred during welding. The brazed long fibre in-plane mesh material, on the other hand, exhibited good welding characteristics, with good current flow from the start of the welding period. The short fibre 3-D array sheet is also readily weldable.

- (f) Overall, it is clear that sheet of this type can offer attractive combinations of light weight, high beam stiffness / strength, good interfacial toughness and low through-thickness electrical resistivity - allowing resistance welding to be carried out easily with conventional equipment. Of the three cores examined, the brazed short fibre 3-D array structure clearly offers the best combination of these properties. Ongoing work is aimed at exploring the influence of core structure on other aspects of sheet performance, including fatigue resistance, formability, energy absorption during crushing and sound / vibration damping characteristics, as well as optimisation of sheet manufacturing procedures. The material is evidently of potential interest to the automotive industry, even though it will inevitably be somewhat more expensive than monolithic metal sheet.

---

## References

1. T.M. McCormack, R. Miller, O. Kesler and L.J. Gibson, "Failure of Sandwich Beams with Metallic Foam Cores", *Int. J. of Solids and Structures*, 38 (28-29) (2001), 4901-4920.
2. C. Chen, A.M. Harte and N.A. Fleck, "The Plastic Collapse of Sandwich Beams with a Metallic Foam Core", *Int. J. Mech. Sci.*, 43 (6) (2001), 1483-1506.
3. A.M. Harte, N.A. Fleck and M.F. Ashby, "Sandwich Panel Design using Aluminium Alloy Foam", *Adv. Engng. Mater.*, 2 (4) (2000), 219-222.
4. T.S. Lok and Q.H. Chen, "Elastic Stiffness Properties and Behavior of Truss-Core Sandwich Panel", *J. Structural Engineering - ASCE*, 126 (5) (2000), 552-559.
5. D.J. Sypeck and H.N.G. Wadley, "Multifunctional Microtruss Laminates: Textile Synthesis and Properties", *J. Mater. Res.*, 16 (3) (2001), 890-897.
6. S. Chiras, D.R. Mumm, A.G. Evans, N. Wicks, J.W. Hutchinson, K. Dharmasena, H.N.G. Wadley and S. Fichter, "The Structural Performance of Near-Optimized Truss Core Panels", *Int. J. of Solids and Structures*, 39 (15) (2002), 4093-4115.
7. R. Gustavsson, "Formable Sandwich Construction Material and Use of the Material as Construction Material in Vehicles, Refrigerators, Boats etc", patent WO 98/01295, 15th Jan. 1998, AB Volvo, International.
8. A.E. Markaki and T.W. Clyne, "Mechanics of Thin Ultra-Light Stainless Steel Sandwich Sheet Material: Part I - Stiffness", *Acta Mater.*, 51 (5) (2003), 1341-1350.
9. A.E. Markaki and T.W. Clyne, "Mechanics of Thin Ultra-Light Stainless Steel Sandwich Sheet Material: Part II - Resistance to Delamination", *Acta Mater.*, 51 (5) (2003), 1351-1357.

10. M. Jou, "Experimental investigation of resistance spot welding for sheet metals used in automotive industry", *JSME Int. J. Series C-Mech. Systems Machine Elements and Manufacturing*, 44 (2) (2001), 544-552.
11. S.S. Babu, M.L. Santella, Z. Feng, B.W. Riemer and J.W. Cohron, "Empirical Model of Effects of Pressure and Temperature on Electrical Contact Resistance of Metals", *Science and Technology of Welding and Joining*, 6 (3) (2001), 126-132.
12. S.C. Wang and P.S. Wei, "Modeling Dynamic Electrical Resistance during Resistance Spot Welding", *J. Heat Transfer - Trans. ASME*, 123 (3) (2001), 576-585.
13. J.A. Khan, L.J. Xu, Y.J. Chao and K. Broach, "Numerical Simulation of Resistance Spot Welding Process", *Numerical Heat Transfer Part A-Applications*, 37 (5) (2000), 425-446.
14. U. Dilthey, H.C. Bohlmann, U. Reigen, W. Sudnik, W. Erofeew and R. Kudinow (1999) "Modelling and Numerical Simulation of Resistance Spot Welding with Experimental Verification", 9th International Conference on the Joining of Materials, Helsingor, Denmark, 38-43.
15. H. Tang, W. Hou, S.J. Hu and H. Zhang, "Force Characteristics of Resistance Spot Welding of Steels", *Welding Journal*, 79 (7) (2000), 175S-183S.
16. Y. Zhou, P. Gorman, W. Tan and K.J. Ely, "Weldability of Thin Sheet Metals during Small-Scale Resistance Spot Welding using an Alternating-Current Power Supply", *J. Electronic Materials*, 29 (9) (2000), 1090-1099.
17. A.E. Markaki, S.A. Westgate and T.W. Clyne (2002) "The Stiffness and Weldability of an Ultra-Light Steel Sandwich Sheet Material with a Fibrous Metal Core", *Processing and Properties of Lightweight Cellular Metals and Structures*, Seattle, A.K. Ghosh, T.D. Claar, and T.H. Sanders (eds.), TMS, 15-24.
18. H. Oberle, C. Commaret, R. Magnaud, C. Minier and G. Pradere, "Optimizing Resistance Spot Welding Parameters for Vibration Damping Steel Sheets", *Welding Journal*, 77 (1) (1998), 8S-13S.
19. B.F. Sorensen, A. Horsewell, O. Jorgensen and A.N. Kumar, "Fracture Resistance Measurement Method for in situ Observation of Crack Mechanisms", *J. Am. Ceram. Soc.*, 81 (3) (1998), 661-669.
20. A.F. Whitehouse, C.M. Warwick and T.W. Clyne, "The Electrical Resistivity of Copper Reinforced with Short Carbon Fibres", *J. Mat. Sci.*, 26 (1991), 6176-6182.
21. E.E. Underwood, *Quantitative Stereology*. 1970, Reading: Addison-Wesley Publishing Company.
22. D. Hull and T.W. Clyne, *An Introduction to Composite Materials*. Cambridge Solid State Science Series, ed. D.R. Clarke, S. Suresh, and I.M. Ward. 1996, Cambridge: Cambridge University Press.
23. C. DiFrancia, T.C. Ward and R.O. Claus, "The Single-fibre Pull-out Test 1. Review and Interpretation", *Composites A*, 27 (1996), 597-612.
24. J.K. Kim, C. Baillie and Y.W. Mai, "Interfacial Debonding and Fibre Pull-out Stresses. Part I - Critical Comparison of Existing Theories with Experiments", *J. Mat. Sci.*, 27 (1992), 3143-3154.